Surface & Coatings Technology 375 (2019) 256–265

Contents lists available at ScienceDirect

Surface & Coatings Technology

journal homepage: www.elsevier.com/locate/surfcoat

Comprehensive porosity determination of combustion-deposited SiO_x thin films and correlation with FTIR signal

B.S.M. Kretzschmar[a,*], E. Wendler[b], A. Heft[a], R. Köcher[a], C. Voigt[b], C. Ronning[b], B. Grünler[a], E. Rädlein[c]

[a] Innovent e.V., Prüssingstraße 27B, 07745 Jena, Germany
[b] Institut für Festkörperphysik, Friedrich-Schiller-Universität Jena, Helmholtzweg 3, 07743 Jena, Germany
[c] Technical University Ilmenau, Gustav-Kirchhoff-Platz 2, 98693 Ilmenau, Germany

ARTICLE INFO

Keywords:
Porosity
Silicon oxide
Combustion chemical vapour deposition
Weighing
Spectral ellipsometry
Rutherford backscattering spectrometry
Fourier transformed infrared spectroscopy

ABSTRACT

Porous silicon oxide thin films were deposited by combustion chemical vapour deposition (CCVD). Depending on the process parameters applied, the layer thickness ranged from 18 to 165 nm, as obtained by profilometry and spectral ellipsometry (SE). The layer morphology was investigated by scanning electron microscopy (STEM) and atomic force microscopy (AFM) revealing roughnesses of the respective films between 0.1 and 42.4 nm. The porosity of the films was determined using weighing, SE, and Rutherford backscattering spectrometry (RBS) with all methods giving similar values. The porosity varied between 21 and 93%. These high porosities can be an effect of voids resulting from pores and roughness. The investigations revealed an open porosity. The received porosities were correlated with FTIR signal. The FTIR signal strength per unit volume Ψ correlates linearly with the porosity. This result can be used as a calibration curve. Thus, the porosity of an unknown silicon oxide layer can be deduced from the measured FTIR signal and the layer thickness. All methods applied here yield a consistent description of the layer properties.

1. Introduction

The investigation of structural properties of deposited thin films for surface modification is one of the main research areas in material science. In the past decades, the material silicon oxide, prepared as porous SiO_x thin film, was often used as insulation and passivation material [1]. Silicon oxide thin films have also gained great interest due to their application as antireflection coating, *e.g.* for photovoltaic modules [2] or as basic material for the growth of nanowires [3]. Different deposition techniques such as reactive high power impulse magnetron sputtering (HIPIMS) [4], electrospinning [5], liquid-phase-deposition [1], Sol-Gel [6,7] and remote plasma-enhanced chemical vapour deposition (RPECVD) [2] have been established to produce porous silicon oxide. Within these deposition processes different precursors, such as monosilane (SiH_4) [2], hydrofluorosilicic acid (H_2SiF_6) [1] or tetraethoxysilane (TEOS) [5], were used. Especially, the HIPIMS and RPECVD techniques are here cost-intensive vacuum-based methods.

The non-vacuum-based combustion chemical vapour deposition (CCVD) process is a very cost effective deposition technique [8]. In contrast to the vacuum-based methods, physical vapour deposition (PVD) and atomic layer deposition (ALD), it is an advantageous method for metal and/or metal oxide deposition. The CCVD process allows changing the deposition parameters, such as substrate temperature, burner passes and substrate velocity for creating ultrathin dense SiO_x layers on glass substrates building an anticorrosive film against leaching [8]. Furthermore this method permits the deposition of thin ZnO layers using zinc nitrate as precursor [9,10]. “Smart Windows” change their colour from colourless to blue in an electrochromic cell. For this application WO_x thin films are another example [10] as well as morphology investigations of Al_2O_3 by varying the temperature of the substrate during CCVD process [11]. As an example, the use of manganese(II)- and cobalt(II) carboxylates as precursors for thin film deposition of Mn_2O_3/Mn_3O_4 and Co_3O_4 show that not only changing controllable parameters have an effect on structure and morphology of the deposited thin films but also the construction of the precursor itself [12]. In addition to metal oxides, also noble metal layers like silver can be deposited by CCVD [13,14].

Porous materials provide the option of filling with a functional material. Some functionalities are, for example, gold nanoparticles for catalysis or thin layers of SnO_2 for gas sensors, where the SiO_x matrix serves to increase the surface area. The porosity is the ratio of the void volume and the bulk volume. Thus, this measure determines the

* Corresponding author.
E-mail address: bk@innovent-jena.de (B.S.M. Kretzschmar).

https://doi.org/10.1016/j.surfcoat.2019.07.020
Received 18 April 2019; Received in revised form 8 July 2019; Accepted 9 July 2019
Available online 10 July 2019

density, which can be *e.g.* measured by weighing of a known volume, as demonstrated by Cobianu and Pavelescu [15]. The density can be also determined from X-ray reflectivity (XRR) measurements, as demonstrated by M. Wormington and C. Russell [16] or Windover and Lu [17] for interlayer dielectric applications. However, for XRR measurements the roughness of the thin films should not be higher than about 5 nm. With Rutherford backscattering spectrometry (RBS) the number of atoms per unit area can be determined and by knowing the layer thickness, the porosity of the layer can be extracted [17–19]. A non-destructive technique for the determination of the porosity is the laser-generated surface acoustic wave characterisation (LASW), which was performed by Murray et al. for low-*k* SiO_x xerogel films [20]. Furthermore, the porosity correlates with the refractive index [21] and thus could be easily detected from optical measurements [22,23].

The aim of this study was to analyse the porosity of silicon oxide thin films deposited *via* the CCVD process by different experimental techniques. The reliable determination of porosity of such films was necessary before executing further experiments to investigate the dependence of morphological properties on the deposition parameters. Therefore, we deposited silica films by varying selected parameters only in order to create different grades of porosity. The morphology of the deposited layers was investigated by atomic force microscopy (AFM) and scanning transmission electron microscopy (STEM). The porosity was determined by applying weighing, spectral ellipsometry (SE) and RBS measurements. Most of the methods depend on deducing porosity from known properties of an ideal structure like bulk density or refractive index. The precision of a direct method like weighing is limited if film thickness is too low and mass differences are smaller than the accuracy of the balance used. To have another opportunity for determination, the observed porosity was compared with data from Fourier transformed infrared spectroscopy (FTIR).

2. Experimental

2.1. Deposition of silicon oxide thin films by the CCVD process

The deposition of the porous silicon oxide layers was carried out using a home built CCVD system, which is schematically depicted in Fig. 1. The main parts of the system are the gas supply unit for generating a propane-air-mixture (white), the aerosol generator (yellow), a burner and a movable and heatable sample holder. The burner was fed with the gaseous fuel-air mixture (propane and air) doped with the liquid precursor hexamethyldisiloxane (HMDSO). The propane air ratio was controlled by a gas supply unit (50 MD-1B) from Sura Instruments GmbH and can be varied between 1:16 and 1: 24, while the temperature of the propane-air flame ranged from 1400 to 2300 °C. HMDSO was sprayed directly into the fuel-air-mixture as aerosol droplets by using an aerosol generator (ATM 220 from Topas GmbH). To produce particles with the atomizer, different nozzle sizes (0.3, 0.5 and 1.1 mm; not shown in Fig. 1) and different system pressures, adjusted by the compressed air (0.2 to 6 bar), can be used.

The maximum speed of the sample holder is 600 mm s^{-1}. The working distance (burner to substrate) can be chosen between 10 and 100 mm. The sample holder is equipped with a heating system and the temperature can be adjusted up to a maximum value of 600 °C.

For deposition a burner of 100 mm width was used. The sample holder was moved through the flame of the burner to create the thin layer. During the deposition process, no additional heating of the sample holder was applied and the sample is only heated by the flame itself. After cooling to ambient temperature, the coated substrates were cleaned in an isopropyl alcohol ultrasonic bath for 10 min. The samples were then rinsed with distilled water and dried with oil-free compressed air. Upon thin film deposition we varied the system pressure, burner to substrate distance, velocity of the substrate holder and the number of burner passes; while all other parameters were set to fixed values, as summarized in Table 1.

2.2. Morphology and chemical composition

The surface roughness R_a of the deposited layers was determined by AFM using an MFP 3D Classic from Asylum Research in tapping mode with the tip type AC160TS-R3. The measured area was 20 × 20 μm².

The preparation and investigation of cross-section lamellas were done with a Helios Nanolab 600i from FEI (now Thermo Fisher Scientific). The DualBeam microscope is combined with a SEM using a field emitter and a liquid Ga ion source for focused ion beam (FIB) preparation. The samples were covered with Pt to create a stable top layer, otherwise the structure could be destroyed during preparation. The cross section was prepared by lift out technique using the Ga ion beam with 30, 16, 8, 5 and 2 keV under use of the micro manipulator.

The chemical composition was obtained by X-ray photoelectron spectroscopy (XPS) depth profiling using a XPS spectrometer AXIS ULTRA^{DLD} (Kratos Analytical Ltd.). The measurements were done using a monochromatic Al K_α X-ray source (1486.6 eV). The spot used was 300 × 700 μm². All photoelectron spectra were collected at take-off angle Θ = 90°. The sputtering was done using monoatomic argon (5 keV) with a raster size of 1.5 × 1.5 mm². The crater depth was measured using an Alpha Step D-600 profilometer from KLA-Tencor.

2.3. Porosity

2.3.1. Weighing

The porosity P is often determined by the ratio of the density from the porous material ρ_p and the theoretical bulk material ρ_0 under the assumption that the density of the material is constant, according to

$$P = \left(1 - \frac{\rho_p}{\rho_0}\right) \cdot 100\%. \quad (1)$$

The density of the porous layer is given by

$$\rho_p = \frac{m_{layer}}{A_{substrate} \cdot d_{layer}}, \quad (2)$$

where m_{layer} is the difference of the mass $m_{substrate}$ before and $m_{sub+film}$ after deposition of the thin film on the substrate. The masses $m_{substrate}$ and $m_{sub+film}$ were determined using a ultra-microbalance SC2 from Sartorius with an accuracy of 0.01 mg. The value d_{layer} is the thickness of the thin film and $A_{substrate}$ is the area of the substrate which is, to a good approximation, the same area as the layer. In our study, we estimated $A_{substrate}$ by

$$A_{substrate} = \frac{m_{substrate}}{\rho_{substrate} \cdot d_{substrate}}. \quad (3)$$

Our substrates were (100) silicon wafers cut into pieces with a size of about 9 cm^2. The density of silicon was taken to be 2.33 g/cm^3 and the thickness was 525 μm. Further, we used a constant value for the density of $\rho_0 = 2.2\ g\ cm^{-3}$ for amorphous silicon oxide. The layer thicknesses d_{layer} were determined using the profilometer Alpha Step D-600. To do so, two samples were coated simultaneously with one of them being partially covered with a piece of silicon in order to create a clear step. The uncoated sample was used for the determination of the mass changes.

2.3.2. Spectral ellipsometry

The reduction of the density of the layer due to its porosity is accompanied by a reduction of the refractive index, n_{layer}, in comparison to that of the theoretical bulk material, n_0. This effect is used for calculating the porosity according to [22,23]

$$P = \left(1 - \frac{({n_{layer}}^2 - 1) \cdot ({n_0}^2 + 2)}{({n_{layer}}^2 + 2) \cdot ({n_0}^2 - 1)}\right) \cdot 100\% \quad (4)$$

The measurements were performed using a SE 850 from Sentech under 50°, 60° and 70° measuring angles applying a wavelength of

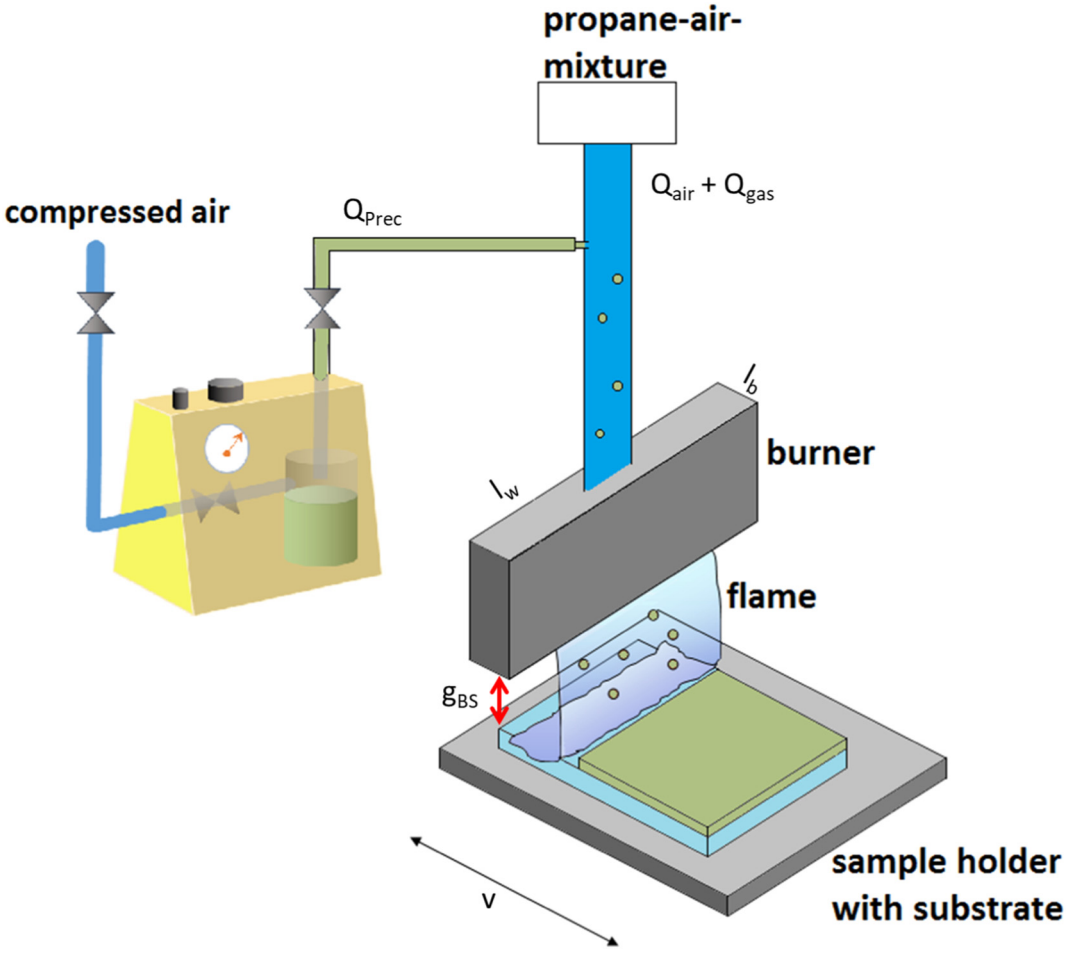

Fig. 1. Schematic CCVD setup.
(Modified from [12]).

Table 1
Deposition parameters for the formation of porous silicon oxide layers using the CCVD process.

Parameter	Value
Flow rate propane [L min^{-1}]	3.6
Flow rate air [L min^{-1}]	70
System pressure of ATM 220 [bar]	1, 3, 5
Distance substrate/burner [mm]	10, 25, 40
Velocity of the substrate holder [mm s^{-1}]	50, 125, 200
Temperature of the substrate holder [°C]	25
Number of passes	2, 4, 6

600 nm. At this wavelength the refractive index of non-crystalline SiO_x is given by $n_0 = 1.458$ [22,23]. The measured quantities were modeled basing on a Cauchy model, with layer thickness and refractive index being the fitted parameters. The layer thickness measured with profilometry was taken as starting value for the fit procedure. After achieving an optimum fit of the measured data, thickness and refractive index of the porous layer are obtained.

2.3.3. Rutherford backscattering spectrometry

Independent measurements of the layer thickness d_{layer} obtained by profilometry and SE can be used for receiving the porosity *via* RBS investigations directly from the relation

$$P = \left(1 - \frac{d_{RBS}}{d_{layer}}\right) \cdot 100\%, \quad (5)$$

where d_{RBS} is the film thickness obtained by the RBS measurements from the measured number of atoms per unit area, Nd_{RBS}, divided by the atomic density of the theoretical bulk material, N. This assumes that the density of the material is known and constant (as with the weighing). The RBS measurements were performed using a 3 MV Tandetron from High Voltage Engineering. The investigations were done under perpendicular ion bombardment and a backscattering angle of 170°. The energy of the He^+ ions was 1.4 MeV. For the evaluation of the RBS spectra the code NDF [24] was applied which is implemented in the local spectra handling software [25]. To ensure random conditions for the crystalline silicon substrate, the samples were tilted by 5° with respect to the incoming beam and rotated around the axis perpendicular to the surface sample. Fitting the measured spectra by calculated ones finally yields the areal atomic density Nd_{RBS} of the deposited layer.

2.3.4. Fourier transformed infrared spectroscopy

FTIR investigations were done using an IR MB 3000 spectrometer from ABB Automation Products GmbH. Scans were carried out with a resolution of 2 cm^{-1} and 32 repeats. The (signal) amplification was 671.41 and the analysed area has a diameter of 2 mm. The background of the spectra was subtracted and the peaks were fitted by Gaussian lines applying OriginPro 8 software.

Weighing, SE and FTIR were performed on one and the same set of samples within a narrow time interval. This ensures almost constant conditions (relative humidity 45% and 25 °C) during measurement and transportation of the samples as well as excludes changes in density or structural changes due to adsorption and desorption of water. There

were no environmental conditions allowed that could have led to phase transitions and thus to changes in density, such as *e.g.* very high temperatures.

3. Results and discussion

3.1. Investigations of layer thickness, morphology and chemical composition

The CCVD process for layer deposition involves complicated reactions, which do not occur at the sample surface only. The propane-air-mixture doped with the precursor gets homogenized in the burner which facilitates a homogeneous flame. Within this flame particles already start to form growing on their way from the burner to the sample surface. The corresponding time is called reaction time. At the start, seed particles form and grow before reaching the surface. Therefore, larger particles are to be expected by increasing the reaction time leading to increased particle diameters and particle agglomerations [26]. Thus, the reaction time t_r is an important parameter, which can be calculated by

$$t_r = \frac{g_{bs} \cdot A_{burner}}{Q_{air} + Q_{gas} + Q_{prec}}, \quad (6)$$

where g_{bs} is the burner to substrate distance, A_{burner} the exit area of the gas (width times depth of the flame) and the denominator is the exit velocity of the gas stream, which is the sum of the volume flow of air Q_{air}, propane Q_{gas} and the precursor Q_{prec} [26].

Another important parameter influencing the morphology and thickness of the deposited layers is the interaction time. This interaction time t_i is given by

$$t_i = \frac{l_b \cdot n_b}{v}, \quad (7)$$

where n_b is the number of burner passes, v the velocity of the sample holder and the burner depth l_b. The burner applied in our experiments yields a constant depth of 10 mm.

By varying the process parameters (see Table 1), we grew in total 17 samples. Depending on the coating parameters, a layer thickness between 18 and 165 nm was achieved. As an example, Table 2 displays coating conditions and obtained layer thicknesses for five representative samples, which are denoted by A to E. Within the experimental uncertainty, profilometric and SE measurements give similar layer thicknesses. SE measurements give a slight tendency to larger thicknesses. This difference can be due to different layer building that may be affected by the cover, because only the profilometry was performed on the partially covered samples. With higher interaction time of the flame with the substrate and silicon wafer cover, the temperature of both increased. This favors the diffusion of the incoming particles on the substrate. The result may be an accumulation and congestion of particles at the substrate and at interface to the silicon cover. Contrary, if the interaction time is short, the cover shadows the building of the step. Because of these effects, the layer thicknesses obtained from SE were used for calculating the porosity by weighing, RBS and FTIR. Thus, all morphology and porosity investigations were performed on the same samples.

Samples A, C and E were prepared with a similar reaction time. Table 2 shows that in this case an increase in the interaction time leads to an increase in the layer thickness. However, different layer thicknesses are observed although the reaction and interaction times are similar by comparing samples B and E. For these two samples a different system pressure was used (not shown). This pressure is set at the aerosol generator (see Sect. 2.1 and Fig. 1) and determines the precursor volume flow Q_p. This in turn influences the processes within the precursor gas, which finally results in the particles seed formation. That is why the low difference in the reaction time between sample B and E has a strong effect on the layer thickness. For coating of sample B, the used system pressure was higher and therefore larger particles were generated. Not all large particles were deposited as an adherent layer. Some particles were removed in the ultrasonic bath, resulting in a reduced layer thickness [26]. Large particles (50–90 nm) are also to be expected in case of sample D because of the long reaction time (see Table 2), which was realized by a larger burner-to-substrate distance (g_{bs}, see Eq. (6)). All other samples in Table 2 were deposited with a g_{bs} which was lower than that of sample D. A similar value of g_{bs} was realized in the former cases (not shown). For the larger particles similar effects occur as described for sample B. This explains the rather low layer thickness of sample D in relation to the long reaction time compared with sample E.

The roughness R_a of the samples was investigated by AFM (see Sect. 2.2). The values of R_a of the samples varied between 0.1 nm and 42.4 nm for the deposited films as displayed in Table 2 for samples A to E. Typical AFM images are shown in Fig. 2 for a more rough surface, sample C (a), and a smoother surface, sample D (b). For sample D evenly distributed hillocks (resulting from particles created during deposition) on the layer can be seen. These hillocks may influence the determination of the layer thickness by profilometry. Thus, the discrepancy of the layer thickness obtained by profilometry and SE may be also an effect of surface roughness.

Fig. 3 shows high-resolution STEM images of the cross section of samples A, C and E. In case of sample A and E, it reveals a compact layer on the silicon surface and a porous structure on the compact layer. Partially the platinum, deposited for protecting the surface, penetrated into the layer. A compact layer could not be observed for sample C. The porous structure consists of agglomerated particles between which there are gaps (here filled with the platinum). This means that the layer structure is formed by growing particle columns. These columns grow with an increasing porosity. Finally, there is a transition from porosity to roughness.

Fig. 4 depicts the chemical composition of sample E obtained by XPS. Before analysis, the adventitious carbon at the surface was removed by sputtering. The figure demonstrates that the composition of the layer does not change with depth. The layer has a slight sub stoichiometry which is ignored. The XPS investigations indicated that the density within the SiO_x agglomerates does not change. A significant difference is not even detected between the porous and the dense part of the layer seen in Fig. 3. This is an important result, because it justifies taking the bulk refractive index of SiO_x for evaluation of the SE measurements. The size of the agglomerates possibly varies over the thickness of the deposited layer. Therefore, the homogeneous composition as shown in Fig. 3 also shows that the density of the agglomerates does not depend on their size. This is one reason why the CCVD process

Table 2
Five samples (A – E) for comparison of layer thickness, interaction time, reaction time and surface roughness of silicon oxide deposited thin films by applying the CCVD.

	A	B	C	D	E
Layer thickness (Profilometry) [nm]	27 ± 2.9	23 ± 3.1	56 ± 8.3	44 ± 4.5	77 ± 7.0
Layer thickness (SE) [nm]	29 ± 2.7	26 ± 3.7	54 ± 4.1	49 ± 5.2	81 ± 3.9
Interaction time [s]	0.4	1.2	0.3	1.2	1.2
Reaction time [ms]	8.0	7.7	8.0	32.0	8.0
Surface roughness R_a [nm]	12.6	0.1	25.0	0.1	42.4

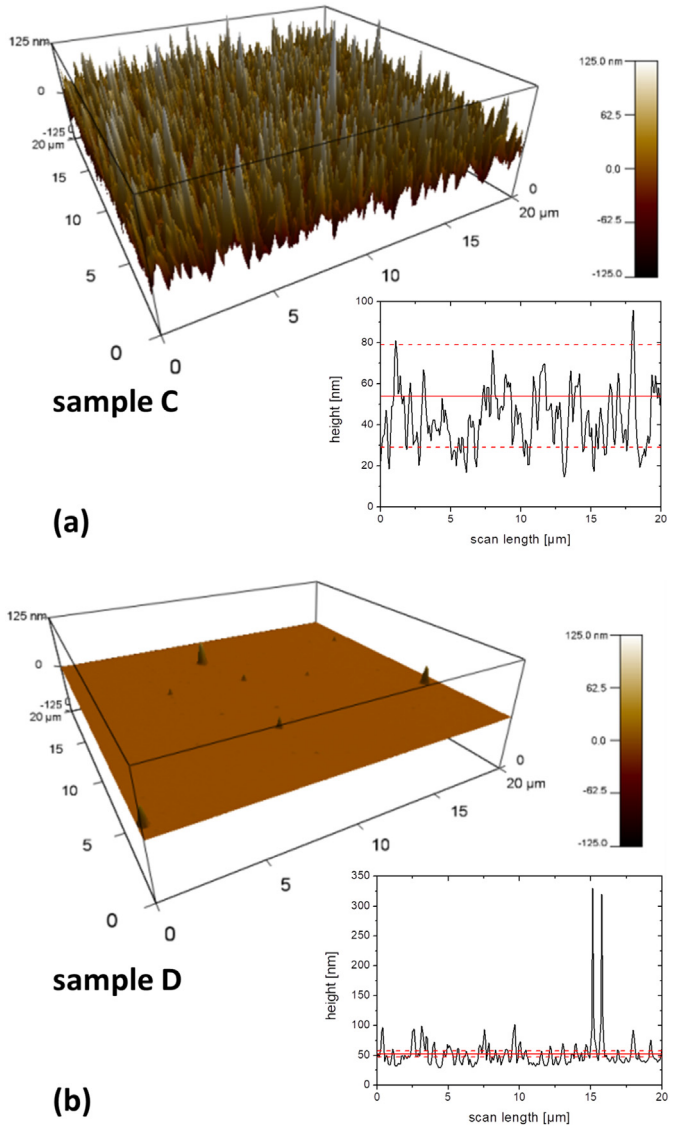

Fig. 2. AFM surface images of silicon oxide thin films C (a) and D (b) as examples of a rough and a smooth layer deposited on a silicon substrate. The respective insets show line scans of representative areas, including hillocks for the case (b).

is a useful technique for deposition of porous SiO_x layers.

3.2. Investigation of the layer porosity

The porosity can be distinguished in open (or effective) porosity and closed (or ineffective) porosity. An open porosity exists when the cavities are connected to each other and to the environment. Conversely, if the cavities are not connected to the environment, there exists a closed porosity. The different methods of measuring the porosity cannot distinguish between open and closed porosity. They only identify a difference in density compared to the bulk material. The morphological investigations performed within this work indicated that the deposited layers have an open porosity. This can be seen, for example, from Fig. 3 which demonstrates that the platinum partially penetrated into the deposited layer.

Fig. 5 displays the SE spectra for sample E. The ellipsometric angles Psi and Delta were collected for three different incidence angles (50°, 60° and 70°) in a wave length range of 350 to 800 nm. To receive the refractive index and the layer thickness, the measured data was fitted. As can be seen from Fig. 5, the simulation is a good approximation to the real data. The thus obtained layer thicknesses are included in Table 2. The obtained values of the refractive index of the layer are used to calculate the porosity applying Eq. (4) (see below).

Fig. 6 shows the RBS spectra for samples C and E. Signals for energies starting at 792 keV result from backscattering of He ions on silicon atoms. Backscattering starting at 508 keV is caused by He ions on oxygen atoms. Because oxygen exists only within a thin layer, the RBS signal appears as peak on top of the silicon signal. For sample E a clear step in the silicon signal at about 760 keV is visible. This marks the change in the relative silicon concentration from about 33% within the deposited layer to the pure silicon substrate. In case of sample C the layer thickness (as seen by RBS) is too thin to resolve the corresponding step. To determine the areal density Nd_{RBS} of the deposited layer, RBS spectra were calculated by NDF [24] and fitted to the measured one. From the XPS analysis it was found that the deposited SiO_x layers are slightly substoichiometric (see Fig. 4). However, the existence of SiO_2 was assumed for the calculation of RBS spectra. For sample C the calculated spectrum fits the data very well. However, there are deviations for sample E at the surface signal from the silicon substrate (at energies around 750 keV) and the trailing edge of the oxygen signal from the layer (around 460 keV). These deviations can be attributed to the roughness of the deposited layer (for details see [27]). The optimum fit of calculated to measured spectra (signal range of the deposited layer) then yields the area density Nd_{RBS} of the deposited layer (see lines in Fig. 6). The porosity, as given in Table 3, is obtained using Eq. (5) with the RBS layer thickness d_{RBS} basing on the bulk atomic density N.

The porosities of the 17 samples were calculated using Eq. (1) (by weighing), 4 (by SE) and 5 (by RBS). For the samples A to E the porosities are presented in Table 3 (RBS measurements were performed for 2 samples, only). The porosity of the samples varied between 21 and 93%. For samples A, B, C and E the porosity determined by the different techniques are the same within the experimental uncertainty. For sample D no satisfactory explanation of the different porosity values can be given. Porosities above 90%, which were obtained for sample D and analysis by weighing, are surprising. This would imply that the layer is not compact, but rather consists of separated particles on the surface only. Indications for that can be seen in the AFM measurements displayed in Fig. 2.

Every individual investigation method is limited in precision causing different results of the layer's real state. The weight of silicon oxide thin films having a thickness of about 20 nm is about 0.022 mg. This small mass change increases the error of the weighing method, because the error increases with decreasing mass. Another problem with weighing is the adsorption of water on the surface, especially in porous layers. This error was minimized by constant environmental conditions during the measurements, as described in section 2.2. Ellipsometry measures the angles Psi and Delta. They describe the change of the polarization state of the reflected light from the samples. The rougher and thinner layers are (< 200 nm; as in our case), the lower the accuracy of ellipsometry. By avoiding certain errors that can be triggered even by the instrument itself, the error can be reduced [28]. Reisinger et al. showed that under certain assumptions, the measurement of very thin SiO_x layers (5–20 nm) with improved accuracy is possible [29]. In their model, the refractive index was kept constant and only the layer thickness was varied. In our model, it was ensured that the layer thickness was varied only within the thickness determined by profilometry and its measurement uncertainty. Since the layer thickness has been determined within narrow limits, the error for determining the refractive index can be reduced. The layer thickness determined by RBS for SiO_x thin films was reported earlier. It was compared to XPS, auger electron spectroscopy (AES), secondary ion mass spectroscopy (SIMS) and transmission electron microscopy (TEM) and showed good agreement, especially for TEM [30]. In comparison to Tougaard and angle resolved XPS (ARXPS), RBS showed a deviation of 30–35% in layer thickness determination, but no reasons for that were given [31]. With RBS measurements, some insecurities including scattering angle

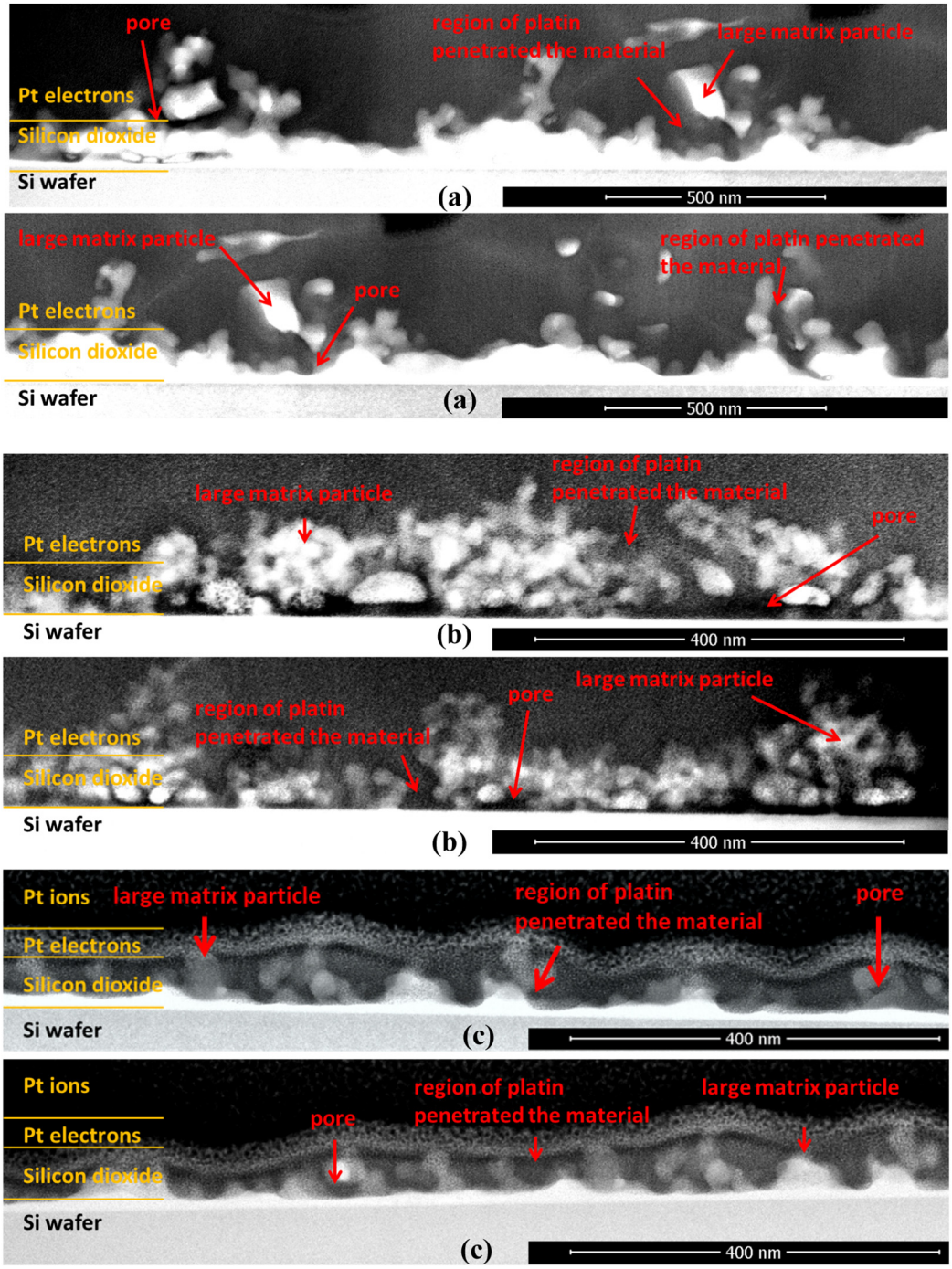

Fig. 3. STEM images of the cross section of silicon oxide thin films (a) A, (b) C and (c) E deposited on a silicon substrate *via* the CCVD process. The images show different areas of the samples.

uncertainty, counting statistics uncertainty and tilted incidence can occur which have led to uncertainties in determining the thickness. These insecurities and how to minimize them were described in Ref. [32]. Kimura and Nakajima demonstrated for SiO_x on Si an uncertainty of the measurement of 15% using the least square method during RBS calculation [33]. All methods determine the integral porosity of the thin film, meaning that an average porosity was calculated. The increasing porosity, as described in Fig. 3, cannot be recorded and calculated in detail using these methods. By combination of these results a good approximation to reality can be obtained.

3.3. Determination of the porosity using FTIR measurements

FTIR measurements are used for chemical structure analysis. Specific peaks are representative for the respective vibration modes. The main vibrations, which occur in SiO_x layers, are listed in Table 4. Beside the peaks located at 1200 cm^{-1}, 1090 cm^{-1}, 935 cm^{-1} and 800 cm^{-1} there is a wagging mode of the Si-O-Si bonding appearing at 450 cm^{-1} [1]. This peak is out of the range of the used spectrometer and will not be considered for the investigations.

FTIR analysis is a quick technique. Additionally such spectrometers are commonly available in laboratories dealing with layer deposition. That is why it would be useful, if the porosity of layers could be

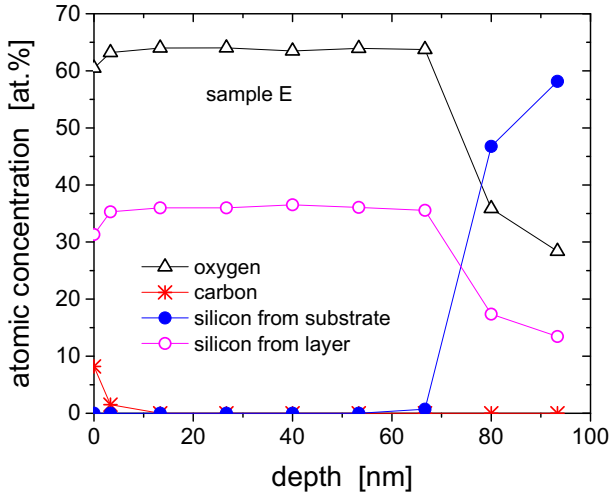

Fig. 4. XPS depth profile of the silicon oxide thin film E deposited on a silicon substrate *via* the CCVD process.

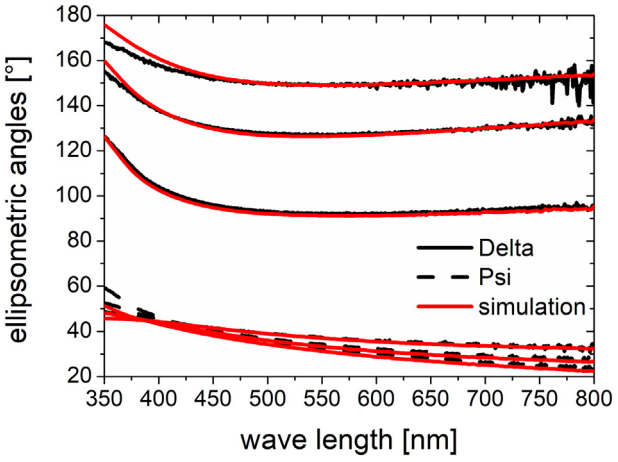

Fig. 5. SE measurements of the silicon oxide thin film E for three different angles of incidence (70°, 60° and 50°); the compact lines are Delta, the dashed lines are Psi and the red lines are the respective simulation. (For interpretation of the references to colour in this figure legend, the reader is referred to the web version of this article.)

determined from this type of analysis. Hints for a correlation between FTIR signal and porosity can be found in the literature already. Gallardo et al. investigated sintered samples by FTIR and plotted the relative absorbance (peak area of TO @ 1090 cm^{-1}/total area of all peaks of the spectrum in the range 1350 to 950 cm^{-1}) over the sintering temperature. They found a decrease of corresponding signals with increasing sintering temperature [36]. It is well known that sintering reduces the porosity. Therefore, the decrease in the relative absorbance should be related to an increase of the porosity. However, in Ref. [36] no comparison with the porosity of the samples is given. A further indication for a correlation between FTIR data and porosity follows from the results in Ref. [37]. In the study, the intensity ratio of the Sh and TO bands (see Table 4) of hybrid silica-titania films (HST) was plotted as a function of volume fraction of porosity [37]. A systematic variation of the FTIR signal with porosity is found. The analysed intensity ratio increased nonlinearly with increasing porosity.

In our investigations, the observed vibration modes can only originate from the deposited layers and not from the underlying silicon substrate. In all cases the entire deposited layer was probed, because the absorption length of the light is much larger than the layer thickness. Layers with the same thickness (measured with profilometry or

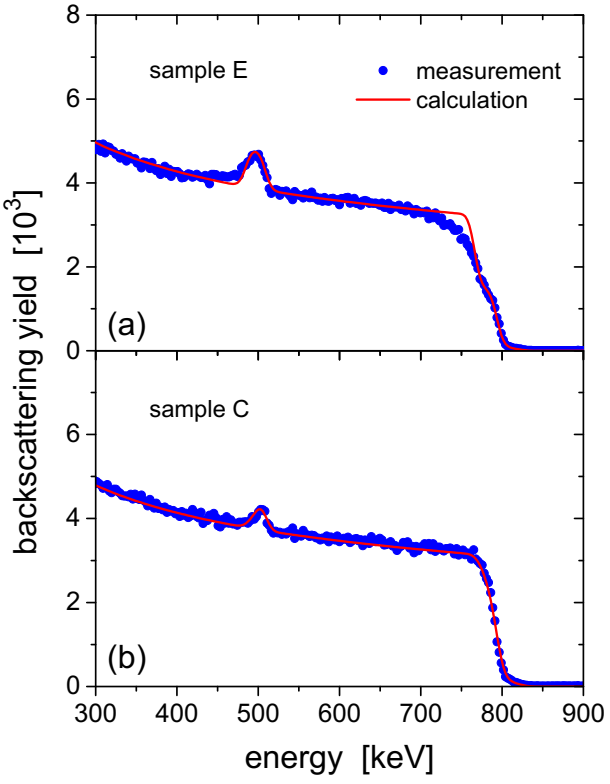

Fig. 6. RBS spectra of different silicon oxide thin layers with different porosities; (a) sample E with a porosity of about 43%; (b) sample C with a porosity of 74%.

Table 3
Comparison of the determined porosities from CCVD deposited silicon oxide layers using weighing, SE and RBS.

Porosity [%]	A	B	C	D	E
Weighing	64 ± 15	21 ± 14	69 ± 10	93 ± 7	36 ± 12
SE	58 ± 8	23 ± 7	80 ± 7	66 ± 6	37 ± 9
RBS	–	–	74 ± 8	–	43 ± 9

Table 4
Vibration modes for a silicon oxide layer.

Name	Location	Ref.
Si-O-Si (Sh)	~1200 cm^{-1}	[34]
Si-O-Si (TO)	~1090 cm^{-1}	[1]
Si-OH	~935 cm^{-1}	[35]
Si-O-Si	~800 cm^{-1}	[1]

SE) but various porosities contain a different mass/amount of SiO_x. The intensity of the FTIR signal depends on the total amount of SiO_x recorded in the analysis. And this in turn depends on the size of the light spot on the sample surface and the area density of SiO_x. This is schematically sketched on the left side of Fig. 7 showing different layer morphologies and their influence on the signal. Compared to the compact layer (a), a decrease in density can result from a rough and open-pore structure (b) or a flat and closed porous structure (c). The third layer (d) shows the volume equivalent layer to the both porous layers. It is to be expected that the total intensity of the FTIR signal decreases with increasing porosity, as shown on the corresponding right side of Fig. 7.

Fig. 8 shows typical FTIR spectra obtained after background

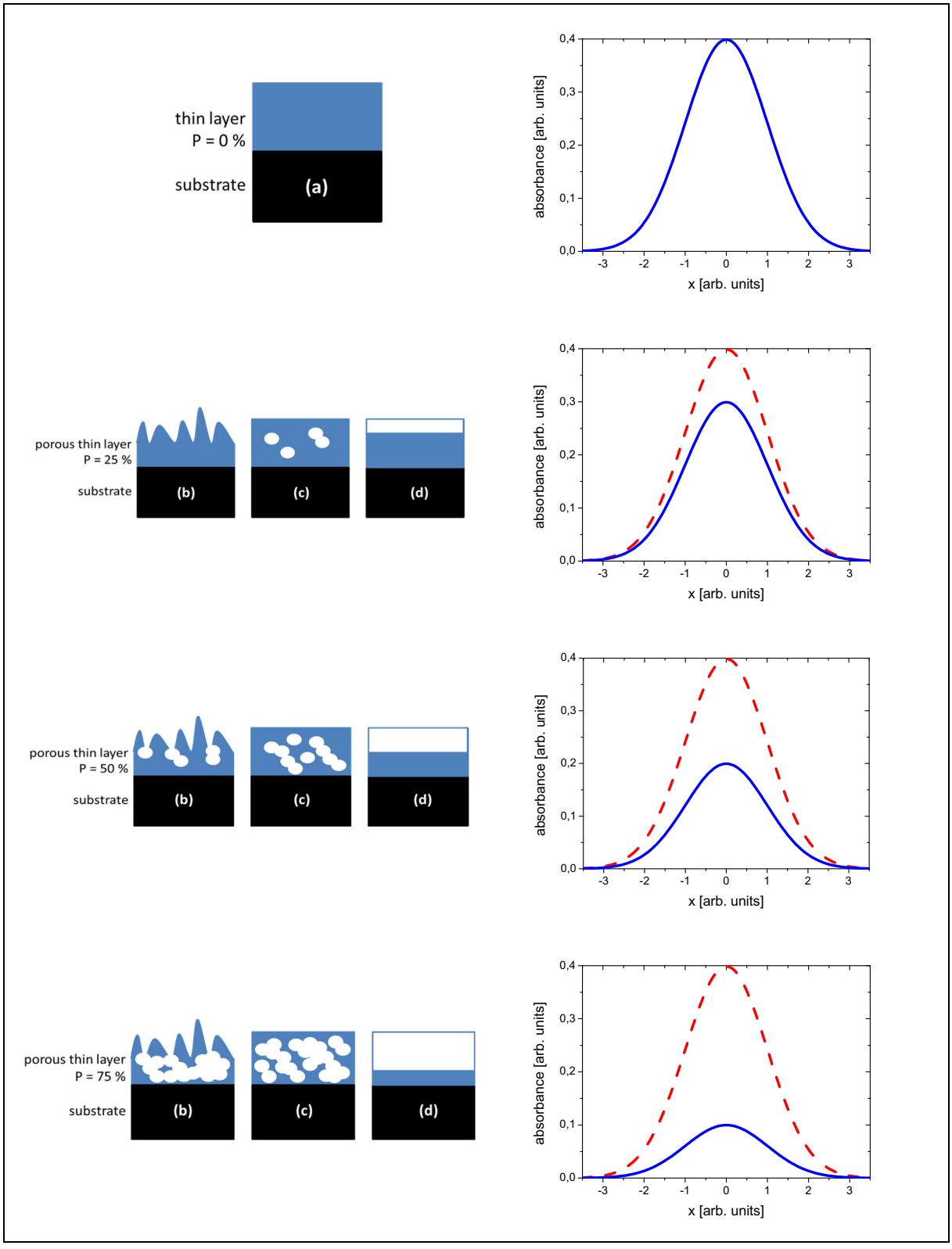

Fig. 7. Schematic representation of the occurrence of different FTIR-signals with increasing porosity.

subtraction. The localised peaks were fitted as explained in Sect. 2.3 (see also [35]). Exemplarily for sample E (c), peaks were observed at 1180 cm^{-1}, 1085 cm^{-1}, 930 cm^{-1} and 810 cm^{-1}, which are in good agreement with data from literature (see Table 4).

In order to quantify the absorbance as measured by FTIR, the signal strength per unit volume Ψ is defined by

$$\Psi = \frac{A_{peak}}{d_{layer} \cdot A_{spot}} = \frac{A_{peak}}{d_{layer} \cdot 1nm^2}, \quad (8)$$

where A_{peak} is the sum of the area under all observed peaks (see Fig. 8) and d_{layer} the layer thickness determined by SE (see Table 2). A_{spot} is the spot size of light beam of the FTIR spectrometer on the sample surface.

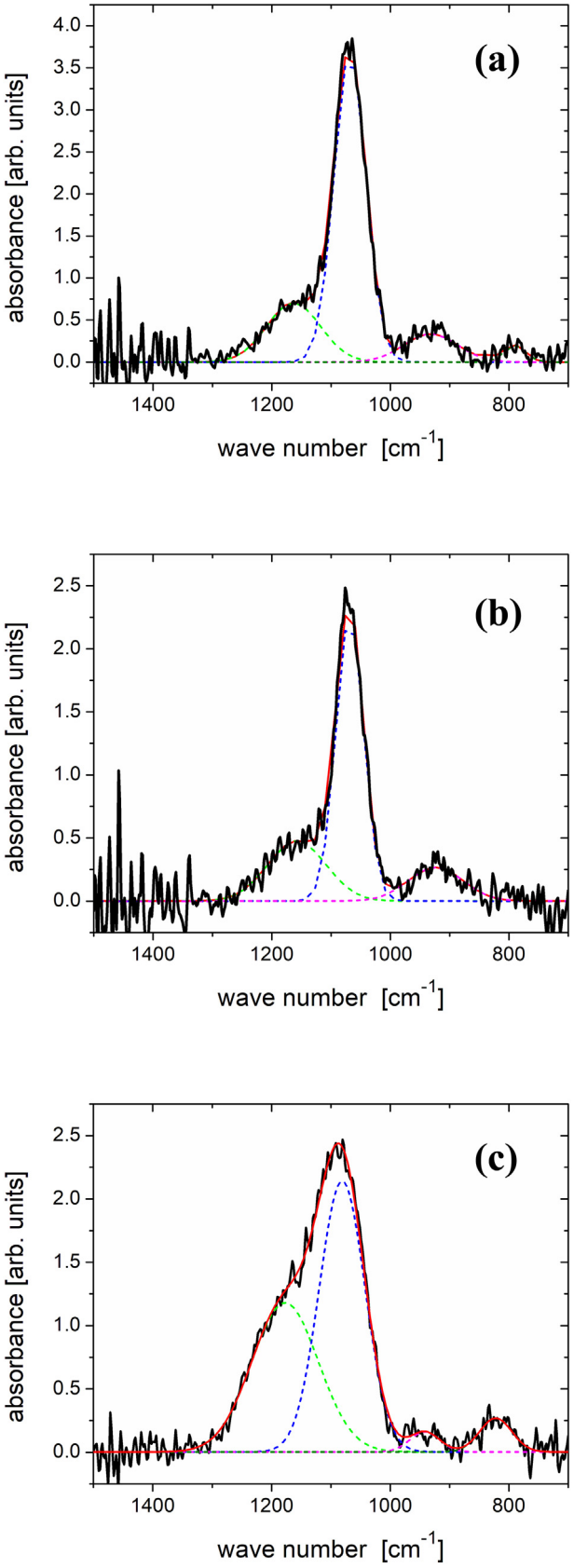

Fig. 8. FTIR absorption spectrum of thin silicon oxide layers B (a), C (b) and E (c) deposited *via* the CCVD process and corresponding Gaussian peak fit. The black line represents the experimental data, the dotted lines are the individually fitted peaks and the red curve is the resultant fit. (For interpretation of the references to colour in this figure legend, the reader is referred to the web version of this article.)

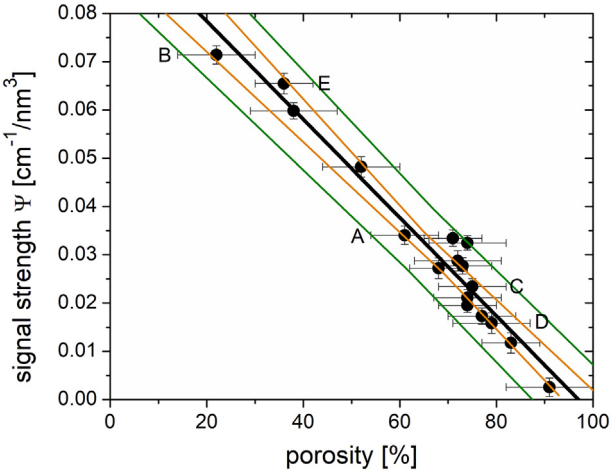

Fig. 9. Correlation between signal strength per unit volume Ψ [cm^{-1}/nm^3] and porosity P [%] for silicon oxide thin films by applying the CCVD process with confidential limits (orange) and prediction limits (green). (For interpretation of the references to colour in this figure legend, the reader is referred to the web version of this article.)

Since A_{spot} is determined by the aperture used, it is the same for all measurements and was set to 1 nm^2 for the calculation of Ψ. The thus obtained value Ψ is an average over the analysed area on the sample surface. The loss of light intensity due to scattering within the porous layers is ignored, because pores > 50 nm were not observed (see Fig. 3).

Fig. 9 shows the relation between Ψ and measured porosity for all 17 layers produced. The used porosity is the average of the obtained porosities using the different methods (weighing, SE and RBS; the deviation of the assumed values results from the maximum uncertainties of the individual measuring methods). Ψ depends on the calculated peak area and the layer thickness and thus the main uncertainty results from the error of determining the layer thickness, which should be much higher than the uncertainty of the peak area calculation. Within the experimental uncertainty, a linear decrease of the signal strength per unit volume (Eq. (8)) with increasing porosity is observed. This is a very interesting and useful result. The intersection of the line is at a porosity of about 97%. In consideration with our uncertainties, this confirms our correlation, at 100% porosity no signal can be obtained. The regression line given in Fig. 9 can be applied as calibration line for a quick estimation of the porosity of silicon oxide layers newly produced with the same system. The parameters of the regression line are a = −0,00102 cm^{-1}/(nm^3%) and b = 0,09876 cm^{-1}/nm^3.

Once such a calibration curve is established, the value of the porosity can be deduced for a new sample with known thickness. In our case, there is a linear dependency, but with other materials and deposition techniques there may be a different correlation and this should be determined and taken into account. However, the value of the porosity alone does not yield complete information about the morphology of the deposited layer. That is why usually further investigations with other techniques are necessary.

4. Summary and conclusion

Combustion chemical vapour deposition was used to prepare silicon oxide thin films with different grades of porosity. It is shown that by applying appropriate conditions during the deposition, a wide variation of layer thicknesses and porosities can be obtained while the stoichiometry of SiO_x is kept constant. This makes this technique suitable for future practical applications. Layer thicknesses were measured by profilometry and SE. Deviations between the results for the two techniques may be caused from the coverage used to create the step for profilometry measurements. Morphology investigations showed a

rough surface arising from agglomerated particles. The porosity was determined using weighing, SE and RBS. The results are in good agreement with each other. Surface roughness and pores influence the measured values of the porosity, but the applied techniques cannot distinguish these effects. We showed a way for determining the porosity by using FTIR. To do this, the significant vibrations for silicon oxide were analysed and an appropriate quantity, the signal strength per unit volume, was defined. This signal strength decreases linearly with increasing porosity for silicon oxide thin films deposited by CCVD. With other materials and deposition techniques there may be a different correlation. When sufficient data are collected, a valid calibration curve is determined. This calibration curve can be used to determine the porosity applying FTIR for a silicon oxide layer of known layer thickness. In this way FTIR can be used as a quick and efficient method for obtaining the porosity. However, the prerequisite for this is to have a corresponding calibration curve. In our case of combustion-deposited silicon oxide the combination of the various experimental techniques gave a good approximation. All methods applied here yields a consistent description of the layer properties.

Compliance with ethical standards

The authors thank Karolina Barnikol from Innovent e.V. for the weighing measurements. The research was funded by the Bundesministerium für Wirtschaft und Energie and the project supporter EuroNorm (MF160129).

Declaration of Competing Interest

The authors declare that they have no conflict of interest.

References

[1] J.-S. Chou, S.C. Lee, Effect of porosity on infrared-absorption spectra of silicon dioxide, J. Appl. Phys. 77 (4) (1995) 1805–1807, https://doi.org/10.1063/1.358877.
[2] H. Nagel, A. Metz, R. Hezel, Porous SiO_2 films prepared by remote plasma-enhanced chemical vapour deposition – a novel antireflection coating technology for photovoltaic modules, Sol. Energy Mater. Sol. Cells 65 (2001) 71–77, https://doi.org/10.1016/S0927-0248(00)00079-9.
[3] I.P. Soshnikov, V.A. Petrov, Y.Y. Proskuryakov, D.A. Kudryashov, A.V. Nashchekin, G.E. Cirlin, R. Treharne, K. Durose, Formation of structures with noncatalytic CdTe nanowires, Semiconductors 47 (7) (2013) 875–878, https://doi.org/10.1134/S1063782613070221.
[4] K. Kim, S. Kim, S. An, G.H. Lee, D. Kim, S. Han, Anti-reflection porous SiO_2 thin film deposited using reactive high-power impulse magnetron sputtering at high working pressure for use in a-Si:H solar cells, Sol. Energy Mater. Sol. Cells 130 (2014) 582–586, https://doi.org/10.1016/j.solmat.2014.08.002.
[5] H.K. Raut, A.S. Nair, S.S. Dinachali, V.A. Ganesh, T.M. Walsh, S. Ramakrishna, Porous SiO_2 anti-reflective coatings on large-area substrates by electrospinning and their application to solar modules, Sol. Energy Mater. Sol. Cells 111 (2013) 9–15, https://doi.org/10.1016/j.solmat.2012.12.023.
[6] W. Glaubitt, P. Löbmann, Antireflective coatings prepared by sol-gel processing: principles and applications, J. Eur. Ceram. Soc. 32 (2012) 2995–2999, https://doi.org/10.1016/j.jeurceramsoc.2012.02.032.
[7] G. Helsch, E. Rädlein, G.H. Frischat, On the origin of the aging process of porous SiO_2 antireflection coatings, J. Non-Cryst. Solids 265 (2000) 193–197, https://doi.org/10.1016/S0022-3093(99)00880-7.
[8] P. Rüffer, A. Heft, R. Linke, T. Struppert, B. Grünler, Characterisation of thin SiO_x-layers on float glass deposited by Combustion Chemical Vapour Deposition (C-CVD), Surf. Coat. Technol. 232 (2013) 582–586, https://doi.org/10.1016/j.surfcoat.2013.06.031.
[9] I. Zunke, S. Wolf, A. Heft, A. Schimanski, B. Grünler, C. Ronning, P. Seidel, Structural properties of zinc oxide deposited using atmospheric pressure combustion chemical vapour deposition, Thin Solid Films 565 (2014) 45–53, https://doi.org/10.1016/j.tsf.2014.06.042.
[10] I. Zunke, A. Heft, P. Schäfer, F. Haidu, D. Lehmann, B. Grünler, A. Schimanski, D.R.T. Zahn, Conductive zinc oxide thin film coatings by combustion chemical vapour deposition at atmospheric pressure, Thin Solid Films 532 (2013) 50–55, https://doi.org/10.1016/j.tsf.2012.11.151.
[11] B.P. Dhonge, T. Mathews, S.T. Sundari, M. Kamruddin, S. Dash, A.K. Tyagi, Combustion chemical vapour deposition of Al_2O_3 films: effect of temperature on structure, morphology and adhesion, Surf. Coat. Technol. 205 (2010) 1838–1842, https://doi.org/10.1016/j.surfcoat.2010.08.026.
[12] B.S.M. Kretzschmar, K. Assim, A. Preuß, A. Heft, M. Korb, M. Pügner, T. Lampke, B. Grünler, H. Lang, Cobalt and manganese carboxylates for metal oxide thin film deposition by applying the atmospheric pressure combustion chemical vapour deposition process, RSC Adv. 8 (2018) 15632–15640, https://doi.org/10.1039/c8ra02288g.
[13] T. Struppert, A. Heft, B. Grünler, Thin functional films by combustion chemical vapour deposition (C-CVD), Thin Solid Films 520 (2012) 4106–4109, https://doi.org/10.1016/j.tsf.2011.06.048.
[14] T. Struppert, A. Jakob, A. Heft, B. Grünler, H. Lang, The use of silver (I)-2-[2-(2-methoxyethoxy) ethoxy] acetate as precursor in the deposition oft hin silver layers on float glass by the atmospheric pressure combustion chemical vapour deposition process, Thin Solid Films 518 (2010) 5741–5744, https://doi.org/10.1016/j.tsf.2010.05.082.
[15] C. Cobianu, C. Pavelescu, Efficiency of the SiH_4 oxidation reaction in chemical vapour deposition of SiO_2 films at low temperature, Thin Solid Films 102 (1983) 361–366, https://doi.org/10.1016/0040-6090(83)90052-4.
[16] M. Wormington, C. Russell, Characterization of porous, low-*k* dielectric thin-films using X-ray reflectivity, AIP Conf. Proc. 683 (2003) 651–655, https://doi.org/10.1063/1.1622540.
[17] D. Windover, T.-M. Lu, Energy-dispersive, x-ray reflectivity density measurements of porous SiO_2, Appl. Phys. Lett. 76 (2000) 158–160, https://doi.org/10.1063/1.125688.
[18] V. Torres-Costa, F. Pászti, A. Climent-Font, R.J. Martín-Palma, J.M. Martínez-Duart, RBS characterization of porous silicon multilayer interference filters, Electrochem. Solid-State Lett. 7 (11) (2004) G244–G246, https://doi.org/10.1149/1.1803052.
[19] J.V. Mantese, A.H. Hamdi, H.W. Sturner, Z.H. Zhang, K.R. Padmanabhan, Porosity and microstructure of thin films of Al_2O_3 formed from alumina sol, J. Electrochem. Soc. 136 (2) (1989) 542–545, https://doi.org/10.1149/1.2096678.
[20] C. Murray, C. Flannery, I. Streiter, S.E. Schulz, M.R. Baklanov, K.P. Mogilnikov, C. Himcinschi, M. Friedrich, D.R.T. Zahn, T. Gessner, Comparison of techniques to characterise the density, porosity and elastic modulus of porous low-*k* SiO_2 xerogel films, Microelectron. Eng. 60 (2002) 133–141, https://doi.org/10.1016/S0167-9317(01)00589-5.
[21] C. Charles, N. Martin, M. Devel, J. Ollitrault, A. Billard, Correlation between structural and optical properties of WO_3 thin films sputter deposited by glancing angle deposition, Thin Solid Films 534 (2013) 275–281, https://doi.org/10.1016/j.tsf.2013.03.004.
[22] İ. Kariper, Structural, optical and porosity properties of CdI_2 thin film, J. Mater. Res. Technol. 5 (1) (2016) 77–83, https://doi.org/10.1016/j.jmrt.2015.10.005.
[23] A. Skoczek, J. Jaglarz, P. Karasiński, Ellipsometric and spectrophotometric investigations of porous silica thin films produced by sol-gel method, Acta Phys. Pol. A 120 (4) (2011) 732–735, https://doi.org/10.12693/APhysPolA.120.732.
[24] N.P. Barradas, C. Jeynes, R.P. Webb, Simulated annealing analysis of Rutherford backscattering data, Appl. Phys. Lett. 71 (1997) 291–293, https://doi.org/10.1063/1.119524.
[25] A. Witzmann, U. Barth, An Interactive Program for RBS-Analysis, FSU Jena, 1989.
[26] I. Zunke, P. Rüffer, T. Tölke, A. Heft, B. Grünler, A. Schimanski, J.M. Grier (Ed.), Combustion: Types of Reactions, Fundamental Processes and Advanced Technologies, 2014, pp. 121–168.
[27] H. Metzner, T. Hahn, M. Gossla, J. Conrad, J.-H. Bremer, Rutherford backscattering spectroscopy of rough films: experimental aspects, Nucl. Inst. Methods Phys. Res. B 134 (2) (1998) 249–261, https://doi.org/10.1016/S0168/S0168-583X(98)00556-4.
[28] H. Reisinger, Minimization of errors in ellipsometric measurements, Solid State Electron. 35 (3) (1992) 333–344, https://doi.org/10.1016/0038-1101(92)90237-7.
[29] H. Reisinger, H. Oppolzer, W. Hönlein, Thickness determination of thin SiO_2 on silicon, Solid State Electron. 35 (6) (1992) 797–803, https://doi.org/10.1016/0038-1101(92)90281-G.
[30] D.A. Cole, J.R. Shallenberger, S.W. Novak, R.L. Moore, M.J. Edgell, S.P. Smith, C.J. Hitzman, J.F. Kirchhoff, E. Principe, W. Nieveen, F.K. Huang, S. Biswas, R.J. Bleiler, K. Jones, SiO_2 thickness determination by x-ray photoelectron spectroscopy, Auger electron spectroscopy, secondary ion mass spectrometry, Rutherford backscattering, transmission electron microscopy, and ellipsometry, J. Vac. Sci. Technol. B 18 (1) (2000) 440–444, https://doi.org/10.1116/1.591208.
[31] B.S. Semak, C. van der Marel, S. Tougaard, Comparison of the Tougaard, ARXPS, RBS and ellipsometry methods to determine the thickness of thin SiO_2 layers, Surf. Interface Anal. 33 (2002) 238–244, https://doi.org/10.1002/sia.1206.
[32] C. Jeynes, N.P. Barradas, E. Szilágyi, Accurate determination of quantity of material in thin films by Rutherford backscattering spectrometry, Anal. Chem. 84 (2012) 6061–6069, https://doi.org/10.1021/ac300904c.
[33] K. Kimura, K. Nakajima, Compositional transition layer in SiO_2/Si interface observed by high-resolution RBS, Appl. Surf. Sci. 216 (2003) 283–286, https://doi.org/10.1016/S0169-4332(03)00386-6.
[34] J.E. Olsen, F. Shimura, Infrared reflection spectroscopy of the SiO_2-silicon interface, J. Appl. Phys. 66 (1989) 1353–1358, https://doi.org/10.1063/1.344435.
[35] R.M. Almeida, C.G. Pantano, Structural investigation of silica gel films by infrared spectroscopy, J. Appl. Phys. 68 (1990) 4225–4232, https://doi.org/10.1063/1.346213.
[36] J. Gallardo, A. Durán, D. Di Martino, R.M. Almeida, Structure of inorganic and hybrid SiO_2 sol-gel coatings studied by variable incidence infrared spectroscopy, J. Non-Cryst. Solids 298 (2002) 219–225, https://doi.org/10.1016/S0022-3093(02)00921-3.
[37] A.M. Seco, M.C. Gonçalves, R.M. Almeida, Densification of hybrid silica-titania sol-gel films studied by ellipsometry and FTIR, Mater. Sci. Eng., B 76 (2000) 193–199, https://doi.org/10.1016/S09215107(00)00442-6.